National Centre for Earth Observation
NATURAL ENVIRONMENT RESEARCH COUNCIL

UNIVERSITY OF LEICESTER

Observing Water Vapour in the Planetary Boundary Layer from the Short-Wave Infrared

Tim Trent[1,2], **Hartmut Boesch**[*1,2], **Peter Somkuti**[3] **& Noëlle A. Scott**[4]

1. Earth Observation Science, Department of Physics & Astronomy, University of Leicester, University Road, Leicester LE1 7RH, UK; 2. National Centre for Earth Observation, Department of Physics & Astronomy, University of Leicester, University Road, Leicester LE1 7RH, UK; 3. Department of Atmospheric Science, Colorado State University, CO, USA; 4. Laboratoire de Météorologie Dynamique, Ecole PolytechniqueCNRS, 91128 Palaiseau, France.

t.trent@leicester.ac.uk

1 Motovation

- The Planetary Boundary Layer (PBL) refers to the lowest region of the atmosphere (100 m to 3000 m) directly influenced by surface processes over both the land and ocean [1].
- Containing ≈80% of the total mass of XH_2O (Fig 1), the PBL regulates the exchange of heat, moisture, momentum, trace gases and aerosols between the Earths surface and the free troposphere [2].
- Evapotranspirative exchange between the PBL and free troposphere is a key component of the water +energy cycle as without the subsequent phase changes most processes would be temperature driven [1].
- Sherwood et al. (2014) [3] found ≈ half the climate sensitivity variance across CMIP5 models is associated with convective mixing between lower & mid-troposphere.
- Rate of mixing & dehydration in PBL impacts development of low-cloud cover impacts albedo.
- Accurate characterisation of heat and water vapour transport is needed to fully describe coupling between surface hydrology, clouds and precipitation [4].
- While work by Millán et al (2016,2019) [5, 6] uses combined MW+NIR imagery for cloudy marine PBL water vapour, no single sensor record of bulk PBL water vapour exists. This work demonstrates the ability of GOSAT to address this gap.

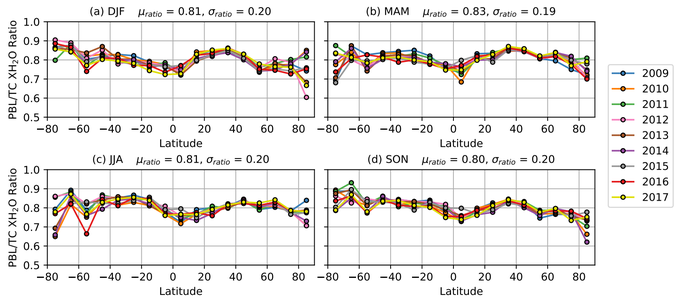

Figure 1: Ratio of PBL to total column (TC) XH_2O concentrations calculated using profiles from the Analyzed Radio Soundings Archive (ARSA). Ratios are shown as a function latitude, year and season, where DJF (December, January, February) is northern hemisphere (NH) winter, MAM (March, April, May) is NH spring, JJA (June, July, August) is NH summer, and SON (September, October, November) is NH autumn. Latitudinal cross sections are shown for each year of the study with the overall ratio mean (μ_{ratio}) and standard deviation (σ_{ratio}) for all years shown in the sub-headings.

2 Estimating PBL Water Vapour

- GOSAT PBL XH_2O is retrieved using the an adapted version of the University of Leicester full physics retrieval (UoL-FP) algorithm [7].
- H_2O windows in bands 2 & 3 chosen to include regions with strong non-saturating, and weaker water vapour absorption lines.

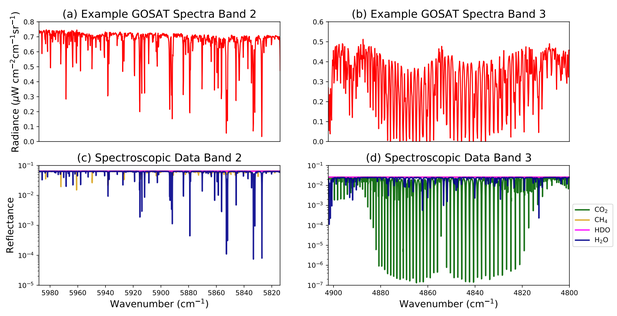

Figure 2: Example GOSAT short wave infrared spectra for bands 2 (**a**) and 3 (**b**). Contribution of main absorbers for bands 2 and 3 are shown in (**c**,**d**) respectively. Spectral lines of absorbers are shown at the native resolution of the spectrascopic database and have not had the GOSAT instrument line shape applied.

- Retrievals contain more than 2 pieces of information - this is exploited to separate out partial columns of XH_2O based on the atmospheric regions resolved by integer values from the trace of the averaging kernel (A) by using Cumulative Degrees-Of-Freedom (CDOF) between the surface and top-of-atmosphere (Fig 3).

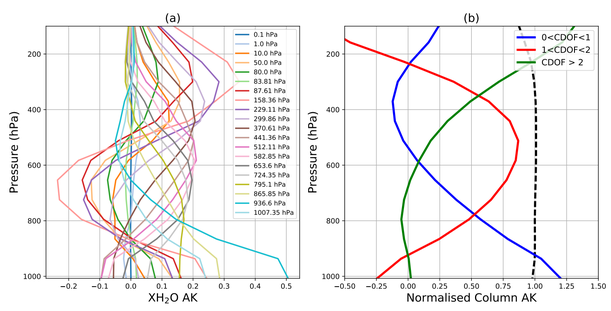

Figure 3: Example of how GOSAT full averaging kernel (AK) is transformed into partial column averaging kernels by exploiting the degrees of freedom in the XH_2O retrieval. An example of the full averaging kernel is shown in panel (**a**) with each level colour-coded. The application of the pressure weighting function to the full averaging kernel is shown in panel (**b**). The column averaging kernel is shown as a dashed black line, while the partial column averaging kernels based on the cumulative degrees-of-freedom (CDOF) being equal to 0–1, 1–2 and greater than 2 are represented by the blue, green and red lines respectively.

- This information is used to modify the pressure weighting function ($\mathbf{h}_{\text{PBL}}$), with levels above where CDOF > 1 set to zero. The closest level in the profile to this point is reffered to as the partial coulmn top pressure (PCTP) and is used as a proxy for boundary layer height.
- The pressure weighting function is then used to calculate the PBL column from the retrieved H_2O profile ($\hat{\mathbf{x}}$):

$$XH_2O_{\text{PBL}} = \mathbf{h}_{\text{PBL}}^{\text{T}}\hat{\mathbf{x}}. \tag{1}$$

- These partial column units are then converted from ppm to g/kg. Examination of global distributions shows clear seasonality (Fig 4).

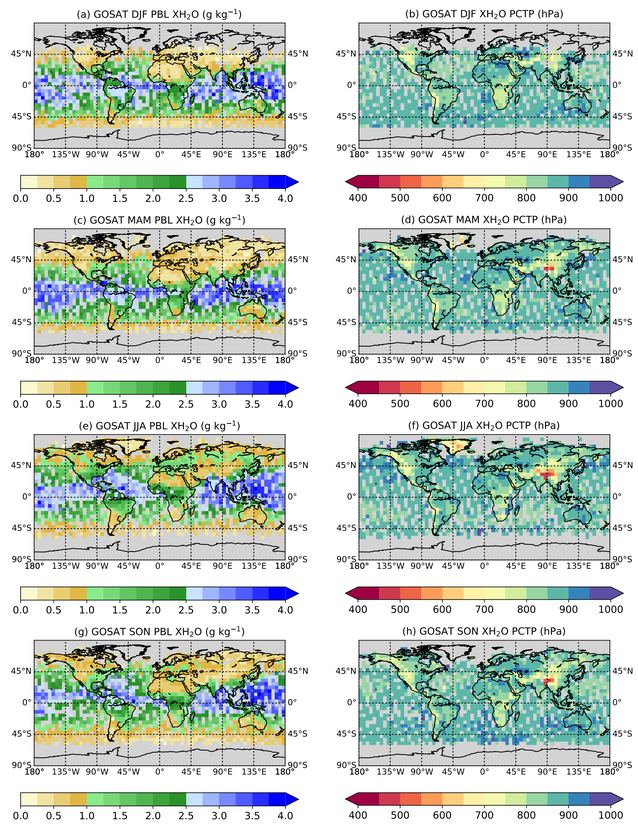

Figure 4: Seasonal distribution of GOSAT PBL XH_2O for northern hemisphere (**a**) winter—December, January and February, (**c**) spring—March, April and May, (**e**) summer—June, July and August, and (**g**) autumn—September, October and November. The corresponding mean seasonal PBL partial column top pressure (PCTP) level values are also shown (**b**,**d**,**f**,**h**). Seasonal plots are based on mean values from December 2016 to November 2017, and are binned in to $5^\circ \times 5^\circ$ averages. The variable spatial sampling of GOSAT introduces a strong seasonal signal, especially over sun glint oceans.

- The a posterior uncertainty ($\hat{\mathbf{S}}$) calculated as part of the retrieval output will be an over-estimation due to the relaxed the H_2O a priori covariance matrix ($\mathbf{S}_{\text{a}}$). Therefore, a second value for the uncertainty in the retrieved PBL XH_2O is calculated from the effects of the instrument noise, instrument smoothing of observed atmospheric state and the interference from the non-target state vector elements [8, 9]:

$$\hat{\mathbf{S}}_{\text{ret}} = \hat{\mathbf{S}}_{\text{m}} + \hat{\mathbf{S}}_{\text{s}} + \hat{\mathbf{S}}_{\text{i}}. \tag{2}$$

- $\mathbf{S}_{\varepsilon}$ can be replaced for an alternative/updated estimate of measurement covariance if required. The uncertainty introduced by the constraint of the state vector on the a priori is described by the smoothing uncertainty covariance matrix and represents the smoothing of the true H_2O profile on the retrieval:

$$\hat{\mathbf{S}}_{\text{i}} = \mathbf{A}_{\text{ue}}\mathbf{S}_{\text{ec}}\mathbf{A}_{\text{ue}}^{T}, \tag{3}$$

- $\mathbf{A}_{\text{ue}}$ are the cross-talk elements of the averaging kernel that relate the response in the target elements to a δ-function perturbation in the non-target elements of the state vector (Rodgers [10]). The non-target uncertainties are described by an ensemble covariance matrix of the true state $\mathbf{S}_{\text{ec}}$. Whilst being represented by a single term, $\hat{\mathbf{S}}_{\text{i}}$ is calculated for each non-target variable (j) and summed together:

$$\hat{\mathbf{S}}_{\text{i}} = \sum_{j=1}^{8} \hat{\mathbf{S}}_{\text{i(j)}}, \tag{4}$$

- Finally, the uncertainty covariances are used to calculate the XH_2O retrieval uncertainty components such that:

$$\sigma_{\text{ret}} = (\mathbf{h}_{\text{PBL}}^{\text{T}}\hat{\mathbf{S}}_{\text{m}}\mathbf{h}_{\text{PBL}})^{\frac{1}{2}} + (\mathbf{h}_{\text{PBL}}^{\text{T}}\hat{\mathbf{S}}_{\text{s}}\mathbf{h}_{\text{PBL}})^{\frac{1}{2}} + (\mathbf{h}_{\text{PBL}}^{\text{T}}\hat{\mathbf{S}}_{\text{i}}\mathbf{h}_{\text{PBL}})^{\frac{1}{2}}, \tag{5}$$

Region	σ_{PBL}		σ_{m}		σ_{s}		σ_{ue}		σ_{Ret}	
	g/kg	%	g/kg	%	g/kg	%	g/kg	%	g/kg	%
Sahara Desert	0.31	11.09	0.12	4.15	0.09	3.07	0.04	1.47	0.24	8.70
Amazon	0.31	10.04	0.09	3.00	0.09	2.77	0.02	0.78	0.20	6.55
Europe	0.30	16.84	0.10	5.80	0.07	4.22	0.03	1.47	0.20	11.49
Greenland	0.29	37.36	0.07	9.49	0.04	4.72	0.01	1.24	0.12	15.46
Sun-Glint Pacific	0.35	9.08	0.09	2.45	0.11	2.75	0.02	0.45	0.22	5.65

Table 1: Retrieval uncertainty components in g/kg and percentage of the retrieved PBL XH_2O for 5 climatic regions for July 2017. The a posterior uncertainties (σ_{PBL}) are the far left-hand column of values, while the updated total retrieval uncertainties (σ_{ret}) are contained in the far right-hand column.

3 Validation against Radiosondes

- GOSAT PBL XH_2O validated against Analyzed RadioSoundings Archive (ARSA) radiosondes between 01/06/2009 - 31/05/2017 (582 sites).
- Collocations are made between ARSA and GOSAT using criteria of 100 km and with 30 mins of sounding, Δpsurf < 5 hPa. Yields ≈ 10k matches.
- GOSAT shows slight wet bias in tropics with a dry bias increase poleward (Fig 5)

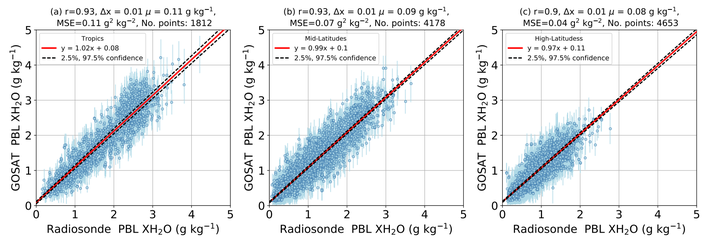

Figure 5: Comparison of GOSAT PBL XH_2O over 3 broad latitudinal bands for same 8 year collocation period (June 2009 to May 2017): (**a**) Tropics (±30°), (**b**) Mid-Latitudes (45°S–30°S, 30°N–45°N) and (**c**). High-Latitudes ($> \pm 45^\circ$).

- To demonstrate that GOSAT can produce proxy values for PBL water vapour we can look at ARSA PBL XH2O using different values for BLH
- Results show good agreement between different definition of PBl water vapour (Fig 6).

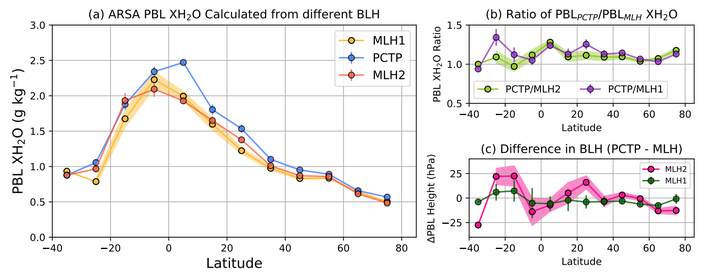

Figure 6: Comparison of mean ARSA PBL XH_2O calculated using the mixing layer height (MLH) derived from; (i) the original radiosonde profile (MLH1), (ii) the partial column top pressure (PCTP) and (iii) MLH derived from the radiosonde profile on the GOSAT retrieval grid (MLH2) as a function of latitude are shown in (**a**). The mean ratio of the PBL XH_2O calculated from the PCTP relative to the MLH as a function of latitude are shown in (**b**). The global mean ratios of PCTP to MLH1 and MLH2 are 1.13 and 1.09 respectively. The mean differences between the PCTP and MLH as a function of latitude are shown in (**c**). All shaded regions and error bars are the respective standard error for each latitudinal bin.

- Consistency of collocations is also assessed using test from Immler et al. [11]:

$$|\mathrm{m}_1 - \mathrm{m}_2| < \mathrm{k} \cdot \sqrt{\sigma^2 + \mathrm{u}_1^2 + \mathrm{u}_2^2}, \tag{6}$$

where m_1 and u_1 are the satellite retrieved water vapour and retrieval uncertainty respectively, and m_2 and u_2 are the radiosonde measured water vapour and measurement uncertainty respectively and (σ) is the collocation uncertainty.

- Fig 7 show the spatial distribution of collocations with radiosonde sites. While collocation numbers are several orders of magnitude lower than IR sounders like AIRS, the K values reduce to 1 in most regions.

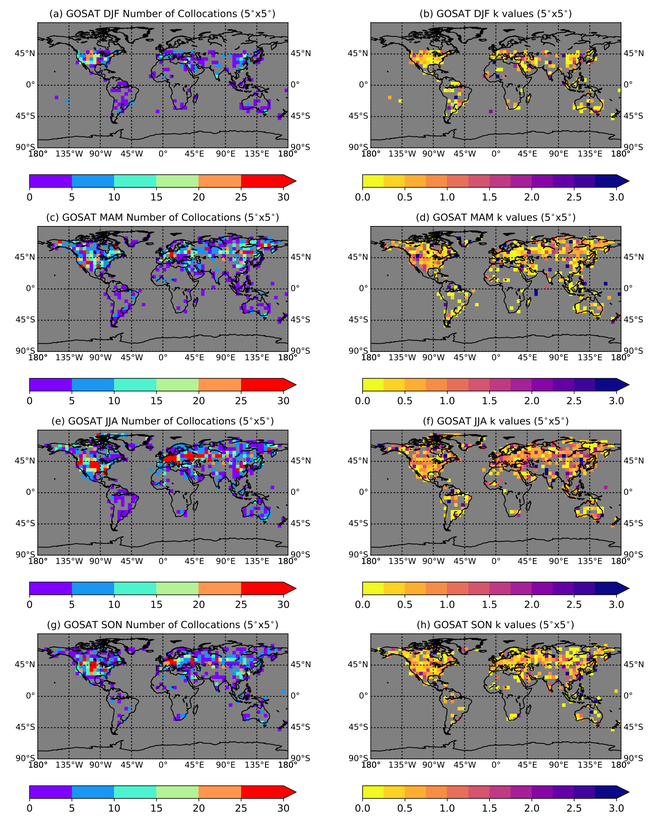

Figure 7: Seasonal collocation and k statistics for GOSAT and ARSA comparisons. Frames (**a**,**c**,**e**,**g**) show global distribution of matched cases as a function of season. North America, Central/Northern Asia and Europe can be seen as the dominate collocation areas. Frames (**b**,**d**,**f**,**h**) show the mean seasonal and global k (Equation (**??**)) value distributions. The majority of $5^\circ \times 5^\circ$ cells reduce to below 2, i.e., they are in statistical agreement (Immler et al. [11]).

4 Outlook

- In our recent study we have shown that a proxy PBL H2O can be retrieved from GOSAT SWIR bands.
- With the exception of high latitudes (dark surface in SWIR) we can retrieve XH2O with low bias (over land) and an accuracy of ≈10%.
- Extension of GOSAT series with launch of GOSAT-2 (2018) & GOSAT-3 (2022) should yield a time series of spanning more than 15 years.

References

[1] R. B. Stull, *An introduction to boundary layer meteorology*, vol. 13. Springer Science & Business Media, 2012.

[2] G. Myhre, D. Shindell, F. Bréon, W. Collins, J. Fuglestvedt, J. Huang, D. Koch, J. Lamarque, D. Lee, B. Mendoza, *et al.*, "Climate change 2013: the physical science basis. contribution of working group i to the fifth assessment report of the intergovernmental panel on climate change," *K., Tignor, M., Allen, SK, Boschung, J., Nauels, A., Xia, Y., Bex, V., and Midgley, PM, Cambridge University Press Cambridge, United Kingdom and New York, NY, USA*, 2013.

[3] S. C. Sherwood, S. Bony, and J.-L. Dufresne, "Spread in model climate sensitivity traced to atmospheric convective mixing," *Nature*, vol. 505, no. 7481, p. 37, 2014.

[4] D. Prieto, P. van Oevelen, M. Rast, S. Senevirantne, and G. Stephens, "ESA-GEWEX EARTH OBSERVATION AND WATER CYCLE SCIENCE PRIORITIES," *proceedings from 'Earth Observation for Water Cycle Science'*, 2015.

[5] L. Millán, M. Lebsock, E. Fishbein, P. Kalmus, and J. Teixeira, "Quantifying marine boundary layer water vapor beneath low clouds with near-infrared and microwave imagery," *Journal of Applied Meteorology and Climatology*, vol. 55, no. 1, pp. 213–225, 2016.

[6] L. F. Millán, M. D. Lebsock, and J. Teixeira, "Variability of bulk water vapor content in the marine cloudy boundary layers from microwave and near-infrared imagery," *Atmospheric Chemistry and Physics Discussions*, vol. 2019, pp. 1–22, 2019.

[7] A. Cogan, H. Boesch, R. Parker, L. Feng, P. Palmer, J.-F. Blavier, N. M. Deutscher, R. Macatangay, J. Notholt, C. Roehl, *et al.*, "Atmospheric carbon dioxide retrieved from the greenhouse gases observing satellite (gosat): Comparison with ground-based tccon observations and geos-chem model calculations," *Journal of Geophysical Research: Atmospheres*, vol. 117, no. D21, 2012.

[8] B. J. Connor, H. Boesch, G. Toon, B. Sen, C. Miller, and D. Crisp, "Orbiting carbon observatory: Inverse method and prospective error analysis," *Journal of Geophysical Research: Atmospheres*, vol. 113, no. D5, 2008.

[9] B. Connor, H. Bösch, J. McDuffie, T. Taylor, D. Fu, C. Frankenberg, C. O'Dell, V. H. Payne, M. Gunson, R. Pollock, J. Hobbs, F. Oyafuso, and Y. Jiang, "Quantification of uncertainties in oco-2 measurements of xco$_2$: simulations and linear error analysis," *Atmospheric Measurement Techniques*, vol. 9, no. 10, pp. 5227–5238, 2016.

[10] C. D. Rodgers, *Inverse methods for atmospheric sounding: theory and practice*, vol. 2. World scientific, 2000.

[11] F. Immler, J. Dykema, T. Gardiner, D. Whiteman, P. Thorne, and H. Vömel, "Reference quality upper-air measurements: Guidance for developing gruan data products," *Atmospheric Measurement Techniques*, vol. 3, no. 5, p. 1217, 2010.